ADVANCED MATERIALS
www.advmat.de

High-Performance Dendrite-Free Lithium Textile Anodes Using Interfacial Interaction-Mediated Ultrathin Metal Organic Framework Multilayers

Donghyeon Nam, Gwonho Yu, Chanseok Lee, Jeongyeon Ahn, Boyeon Kim, Sungha Choi, Keun Hee Kim, Donghyeok Roh, Hyewon Kang, Jeong Gon Son, Hyung-Jun Koo, Jieun Lee, Seoin Back, Seung Woo Lee,* Yongmin Ko,* and Jinhan Cho**

Lithium (Li) metal batteries are among the most promising candidates for next-generation high-energy-density battery systems. Their wider adoption, however, is hindered by safety and stability issues, primarily due to the uncontrollable growth of Li dendrites. Herein, a high-performance dendrite-free Li textile anode is introduced for high capacity and long-term stability using interfacial interaction-mediated ultrathin metal-organic framework (MOF) multilayers. The repeated coordination bonding-based layer-by-layer (LbL) assembly of Ag ions and trithiocyanuric acid (TCA) generates uniform and ultrathin MOF multilayers with a thickness of less than 40 nm on Ni-electroplated polyester textiles. During electrochemical operations, Ag ions in the MOF are chemically reduced in situ to form highly lithiophilic Ag nanoparticles (NPs) without requiring any additional treatment, which significantly lowers the Li nucleation energy barrier. Additionally, the organic TCA in the MOF structure promotes the formation of a Li_3N-rich solid electrolyte interphase layer, thereby enhancing stability over 2000 h (at 1 mA cm^{-2}) in a symmetric cell configuration. Furthermore, a full cell with a $LiFePO_4$ cathode demonstrates remarkable capacity retention of ≈96.5% after 1300 cycles at 1 C. The approach underscores the critical role of interfacial interactions and ultrathin lithiophilic layers in advancing the performance of Li metal batteries.

1. Introduction

The development of high-energy-density batteries is crucial for advancing next-generation energy storage technologies. Li metal stands out as a particularly promising anode material, boasting an exceptionally high theoretical capacity of 3860 mAh g^{-1} and a low electrochemical potential of −3.040 V versus the standard hydrogen electrode.[1–3] However, the practical application of Li metal anodes (LMAs) faces significant hurdles. The primary challenge is the formation of Li dendrites during charge-discharge cycles, which poses severe safety risks, including the possibility of internal short circuits and thermal runaway.[4,5] Additionally, the solid electrolyte interphase (SEI) layer on Li metal is susceptible to continuous fractures and degradation, exacerbated by significant volume changes—≈4.8 µm mAh cm^{-2}—during the processes of Li plating and stripping.[6] These issues lead to capacity loss and diminished

D. Nam, C. Lee, J. Ahn, B. Kim, S. Choi, J. Cho
Department of Chemical and Biological Engineering
Korea University
145 Anam-ro, Seongbuk-gu, Seoul 02841, Republic of Korea
E-mail: jinhan71@korea.ac.kr

G. Yu, J. G. Son, S. Back, J. Cho
KU-KIST Graduate School of Converging Science and Technology
Korea University
145 Anam-ro, Seongbuk-gu, Seoul 02841, Republic of Korea
E-mail: sback@korea.ac.kr

The ORCID identification number(s) for the author(s) of this article can be found under https://doi.org/10.1002/adma.202508218

DOI: 10.1002/adma.202508218

D. Nam, K. H. Kim, D. Roh, H. Kang, S. W. Lee
The George W. Woodruff School of Mechanical Engineering
Georgia Institute of Technology
Atlanta, GA 30332, USA
E-mail: seung.lee@me.gatech.edu

J. G. Son
Soft Hybrid Materials Research Center
Korea Institute of Science and Technology (KIST)
5 Hwarang-ro 14-gil, Seongbuk-gu, Seoul 02792, Republic of Korea

H.-J. Koo
Department of Chemical & Biomolecular Engineering
Seoul National University of Science and Technology
232 Gongneung-ro, Nowon-gu, Seoul 01811, Republic of Korea

J. Lee
Energy Storage Research Center
Korea Institute of Science and Technology (KIST)
5 Hwarang-ro 14-gil, Seongbuk-gu, Seoul 02792, Republic of Korea

S. Back
Prof. S. Back, Department of Integrative Energy Engineering
Korea University
145 Anam-ro, Seongbuk-gu, Seoul 02841, Republic of Korea

cycle life, presenting substantial barriers to the commercialization of LMAs.

To overcome these challenges, researchers have explored a variety of strategies, including the development of novel electrolytes, the engineering of artificial SEI layers, and the modification of separators.[7–14] In addition to these approaches, 3D self-standing current collectors with high electronic conductivity and large surface area stand out for their ability to suppress dendrite growth.[15–17] These current collectors function as 'Li cages', accommodating the volume expansion of the Li layer during charge-discharge cycling and effectively reducing local current density. This arrangement not only promotes uniform Li deposition but also boosts electrochemical stability. Specifically, the augmentation of the effective surface area afforded by 3D-structured hosts serves to mitigate the concentration polarization of Li ions at the electrolyte/electrode interface, promoting a more homogeneous interface energy distribution. That is, these structural characteristics establish a well-defined ion diffusion network, reducing the risk of Li^+ ion depletion or large concentration gradient at the electrode/electrolyte interface. This effect prolongs the Sand's time, thereby delaying the critical threshold that initiates Li dendrite formation.[18]

While the porous structures of the 3D hosts ensure uniform ion flux, the Li nucleation process is strongly influenced by surface energy. In other words, Li ions preferentially adsorb onto lithiophilic sites that provide strong binding interactions, thus reducing the total Gibbs free energy of the battery system.[19] However, commonly used current collectors such as copper (Cu) and nickel (Ni) exhibit poor interfacial wettability with Li, which leads to high nucleation overpotentials and non-uniform Li deposition. To mitigate these issues, lithiophilic metals (i.e., Ag, Zn, and Au) and metal oxides (i.e., Ag_2S, NiO, and Co_3O_4) have been introduced onto lithiophobic current collectors (i.e., Cu or Ni) to promote uniform Li nucleation and suppress dendritic growth by lowering the nucleation barrier.[20–24] Despite the effectiveness of these approaches, they have primarily been demonstrated on 2D current collectors. Applying such strategies to highly porous 3D current collectors introduces new challenges, particularly in achieving uniform surface modification throughout the complex and tortuous internal structure. That is, a key challenge in utilizing a 3D porous current collector is the uniform integration of lithiophilic components. Unlike conventional flat 2D electrodes, 3D current collectors present a large, intricate surface area that is difficult to coat evenly. Traditional deposition methods such as slurry casting and electroless plating (or chemical reduction) often fail to provide uniform and controlled deposition, leading to irregular Li nucleation and plating behavior.[25–28] Particularly, slurry casting poses additional limitations. The inclusion of insulating polymer binders in thick slurry layers (ranging from several to tens of μm) can significantly reduce the porosity and hinder ion transport, thereby limiting the potential performance improvement.[29] Compounding the challenge, non-uniform deposition may create regions that are either oversaturated or undercovered with lithiophilic material, disrupting uniform Li growth and increasing the risk of localized Li accumulation and unstable deposition.

Another major challenge associated with lithiophilic component-modified 3D hosts lies in their extensive surface area, which significantly increases the Li/electrolyte interface.[30] This expanded interface can accelerate the formation of the solid electrolyte interphase (SEI) layer, often leading to excessive and unstable SEI layers. Such thick and uneven SEI layer formation not only increases interfacial resistance but also reduces the effective capacity of lithium metal anodes (LMAs), thereby impairing overall battery performance. The structural integrity and electrochemical stability of the SEI layer are primarily governed by its chemical composition, which determines ion transport, mechanical robustness, and interfacial compatibility with the electrolyte.[31,32] For instance, inorganic compounds, such as lithium nitride (Li_3N), exhibit high ionic conductivity ($\approx 10^3$ S cm^{-1}) and superior mechanical strength compared to organic components.[33–35] These characteristics enable the formation of dense, uniform SEI layers that effectively block Li dendrite growth and maintain interfacial stability. Therefore, engineering a high-quality SEI layer is considered a key strategy for unlocking the full potential of 3D porous current collectors in high-performance LMAs, as it addresses both safety and longevity while enabling stable cycling.

In this study, we introduce a dendrite-free, high-performance Li textile anode (LTA) that enables LMAs with high capacity and long-term stability through the use of interfacial interaction-mediated metal-organic framework (MOF) multilayers and Ni-electroplated polyester textile (**Scheme 1**). Our approach leverages a novel deposition technique in which ultrathin (<40 nm) lithiophilic MOF multilayers are conformally assembled onto a highly porous textile current collector. This is accomplished via a coordination bonding-induced layer-by-layer (CB-LbL) assembly process, ensuring uniform ion flux throughout the electrode. A key advantage of this method is its ability to uniformly deposit MOF architectures across the entire surface of the textile collector by repeatedly alternating Ag^+ ions and the organic linker, trithiocyanuric acid (TCA), at room temperature. This eliminates the need for additional complex synthesis steps typically required in conventional MOF fabrication.[36–38] Notably, most prior studies on MOFs have focused on separator modification—typically via slurry coating—to homogenize current distribution across the LMA[39–41] (Table S1, Supporting Information). In contrast, our approach introduces an ultrathin MOF layer directly onto the textile current collector via CB-LbL assembly, serving as a lithiophilic interfacial layer. This technique enables precise control over the composition, uniformity, and mass density of the $[Ag^+/TCA]_n$-MOF multilayer at the nanometer scale, optimizing the interface for enhanced LMA performance. Moreover, while previous studies have mainly attributed the effect of MOFs on LMA performance to the organic segments interacting with Li^+ ions and the electrolyte, our findings reveal an additional, synergistic mechanism: during electrochemical cycling, Ag^+ ions within the MOF are chemically reduced to form lithiophilic Ag nanoparticles (Ag NPs), which significantly lower the

Y. Ko
Division of Energy & Environmental Technology
Materials Research Institute
Daegu Gyeongbuk Institute of Science and Technology (DGIST)
333 Techno Jungang-daero, Hyeonpung-eup, Dalseong-gun, Daegu 42988, Republic of Korea
E-mail: yongmin.ko@dgist.ac.kr

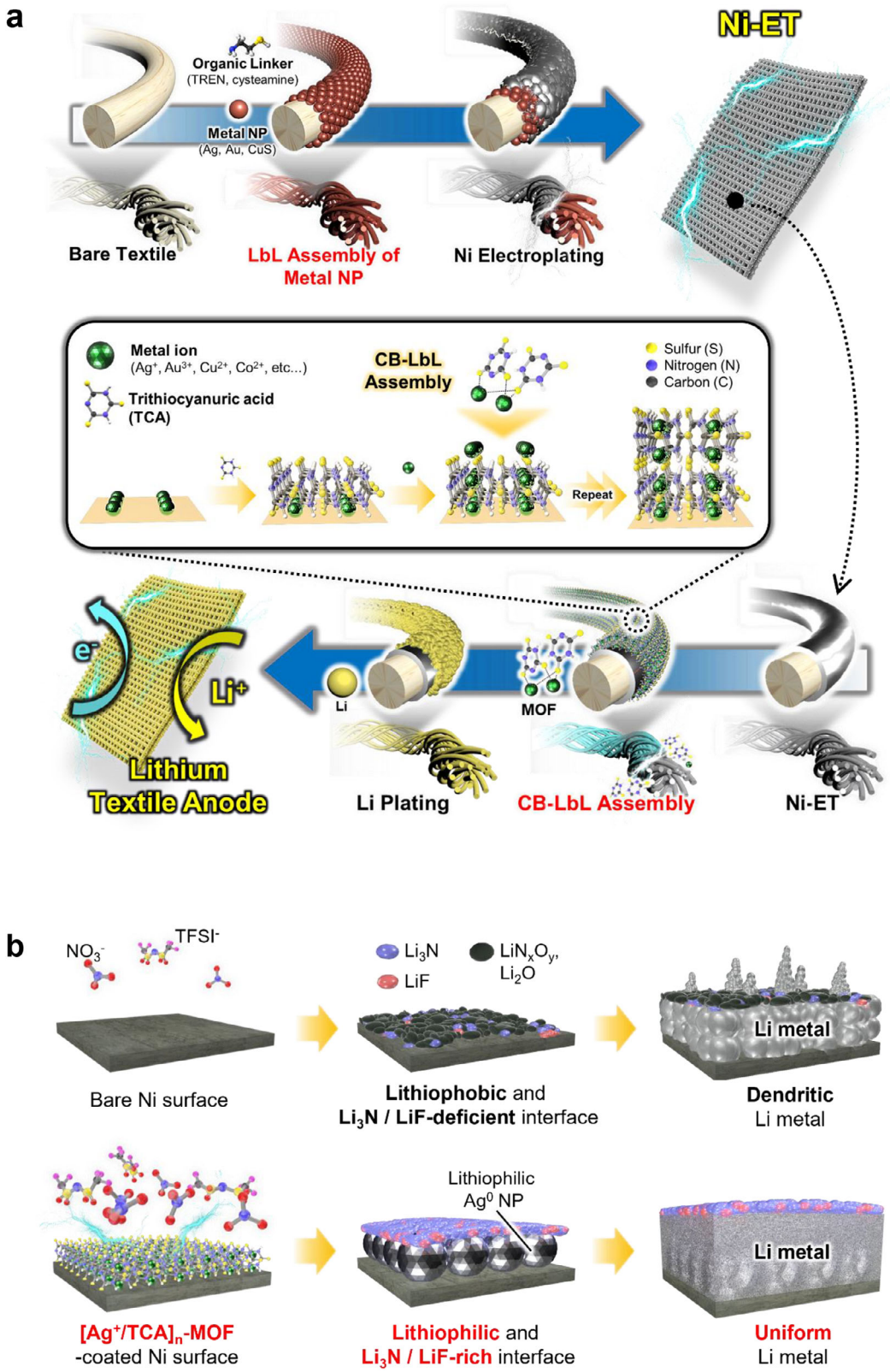

Scheme 1. Schematic illustration. Schematic illustration for the preparation of Li metal textile using interfacial interaction-mediated ultrathin MOF multilayers.

Li nucleation barrier.[36,42,43] Furthermore, the coordinated TCA molecules within the MOF multilayers generate surface dipoles that attract anions from the inner Helmholtz plane, facilitating the formation of an anion-dominated SEI layer comprising Li_3N-rich compounds.[44–46] Thus, the $[Ag^+/TCA]_n$ MOF multilayers act as a multifunctional interfacial layer that not only promotes homogeneous Li plating at the substrate/Li interface but also catalyzes the formation of a thin, dense, and highly ion-conductive SEI layer. More specifically, the novelty of our study lies in the implementation of a well-defined interfacial CB-LbL assembly strategy, which enables the in-situ formation of an ultrathin and highly lithiophilic Ag NP layer onto the host electrode without the need for additional chemical synthesis. This method further offers precise, molecular-level control over both the physical architecture (e.g., thickness, uniformity) and the chemical functionality of the MOF-based multilayer.

To realize this goal, we preferentially fabricated a conductive polyester textile by employing a ligand exchange-induced LbL assembly process using metal NPs such as Ag NPs, CuS NPs, and Au NPs along with amine-functionalized molecular linkers—specifically tris(2-aminoethyl)amine (TREN) (Scheme 1a). Notably, the polyester textile, composed of numerous intertwined fibers, offers a significantly larger surface area compared to conventional 3D current collector materials such as Ni foam. This metal NP assembly not only transforms the intrinsically insulating textile into a conductive substrate but also enables its compatibility with subsequent nickel (Ni) electroplating. As a result, a highly porous 3D textile current collector with an extremely large surface area was successfully constructed. While the resulting Ni-ET provides a conductive and porous framework that facilitates efficient current distribution, its inherently low lithiophilicity makes it less suitable for uniform lithium deposition compared to Ag NP-modified systems.

To overcome this limitation, we coated the Ni-ET with $[Ag^+/TCA]_n$ MOF multilayers, which offer high lithiophilicity arising from the COOH groups of TCA and the in-situ formation of Ag NPs during electrochemical operation, while maintaining the conductive porous architecture that promotes uniform curren distribution (Scheme 1b). Specifically, CB-LbL assembly was carried out between Ag^+ ions and the thiol and amine functional groups of TCA, forming $[Ag^+/TCA]_n$-MOF multilayers directly on the Ni-electroplated textile collector. The resulting MOF-coated substrate (i.e., $[Ag^+/TCA]_n$ MOF-coated Ni-electroplated textile), termed "*n*-MOF-Ni-ET", was subsequently electroplated with Li to form the functional anode (Li-*n*-MOF-Ni-ET). Importantly, the porous architecture of the original polyester textile was fully preserved throughout all processing steps, including metal NP deposition, electroplating, and MOF assembly. Among these, the Li-5-MOF-Ni-ET anode demonstrated particularly outstanding performance, achieving a Coulombic efficiency of 99.1% at 600 cycles at a current density of 1 mA cm^{-2} and an areal capacity of 1 mAh cm^{-2}. In a symmetric cell configuration, this LTA (i.e., Li-5-MOF-Ni-ET) exhibited stable cycling performance for over 2000 h under the same conditions. Furthermore, when paired with a lithium iron phosphate ($LiFePO_4$, LFP) cathode in a full cell configuration with a low N/P ratio of 1.4, the system delivered excellent cycling retention of 92% over 180 cycles, as well as robust electrochemical performance in a Li-5-MOF-Ni-ET/LFP-based pouch cell. Although the increased total mass of porous textile-based host electrodes relative to thin Ni foil may negatively affect energy density, it is important to note that the resulting MOF-Ni-ET provides an exceptionally large lithiophilic surface area. This feature effectively lowers the local current density, thereby significantly enhancing operational stability. Given the effectiveness of ultrathin lithiophilic MOF layers based on CB-LbL assembly for high-performance, dendrite-free LMAs, our approach holds significant promise for the development of advanced LMAs.

2. Results and Discussion

2.1. Ni-textile Current Collector Using LbL-Assembled Metal NP Multilayers

For preparing highly conductive textile current collectors as depicted in **Figure 1a**, we initially synthesized tetra(octyl ammonium) (TOA) stabilized-Ag NPs with an average diameter of ≈8 nm in toluene (Figure 1b; Detailed Experimental Section, Supporting Information). These TOA-Ag NPs were then subjected to an in situ ligand exchange reaction with TREN molecules ($M_w \approx 146$) containing amine (NH_2) groups. In this process, the loosely bound bulky TOA ligands on the Ag NP surface were replaced by NH_2 groups of TREN, which were confirmed by Fourier transform infrared (FTIR) spectroscopy (Figure S1, Supporting Information). Additionally, the organic molecular linker, consisting of a single, small TREN molecule, effectively reduced the distance between adjacent Ag NPs. To verify this, we analyzed the optical properties of LbL-assembled $[TOA\text{-}Ag\ NP/TREN]_n$ multilayers with increasing bilayer numbers using UV–vis spectroscopy (Figure 1c). Notably, the characteristic surface plasmon peak of TOA-Ag NPs dispersed in toluene at 418 nm (indicated by a red dashed line in Figure 1c) completely vanished after the deposition of one bilayer (i.e., $n = 1$), indicating a significant decrease in the interparticle distance both laterally and vertically.

As the bilayer number (n) of $[TOA\text{-}Ag\ NP/TREN]_n$ multilayers increased from 1 to 3 onto polyester textile with a thickness of ≈150 µm, the sheet resistance of the modified textiles significantly decreased, from ≈550 to 0.05 Ω sq^{-1} (Figure 1d). This reduction in sheet resistance enabled the subsequent electroplating of Ni. Specifically, for the $[TOA\text{-}Ag\ NP/TREN]_2$ multilayers, which exhibited a sheet resistance of ≈5.2 Ω sq^{-1}, an additional Ni electroplating process further lowered the sheet resistance to $\approx 1.1 \times 10^{-3}$ Ω sq^{-1} (with an electrical conductivity $\approx 2.52 \times 10^4$ S cm^{-1}). This indicates the formation of a highly conductive Ni layer on the surface of the $[TOA\text{-}Ag\ NP/TREN]_2$ multilayer-coated polyester fibers. Moreover, this Ni-electroplated textile (Ni-ET) maintained the highly porous structure of the original polyester, as the LbL-assembled Ag NP multilayers were uniformly deposited across numerous polyester fibers, followed by selective, uniform coating of a Ni layer (thickness ≈800 nm) on the conductive fibers, as shown in Figure 1e. Given that the primary function of Ni electroplating is to enhance electronic conductivity, other electrochemically stable metals with high conductivity—such as copper (Cu)—could also be used for this purpose (Figure S2, Supporting Information). The electroplated Ni layer included crystalline nickel hydroxides such as α-$Ni(OH)_2$ and β-$Ni(OH)_2$ as well as metallic Ni (Ni^0 state) on the surface, which was confirmed by X-ray photoelectron

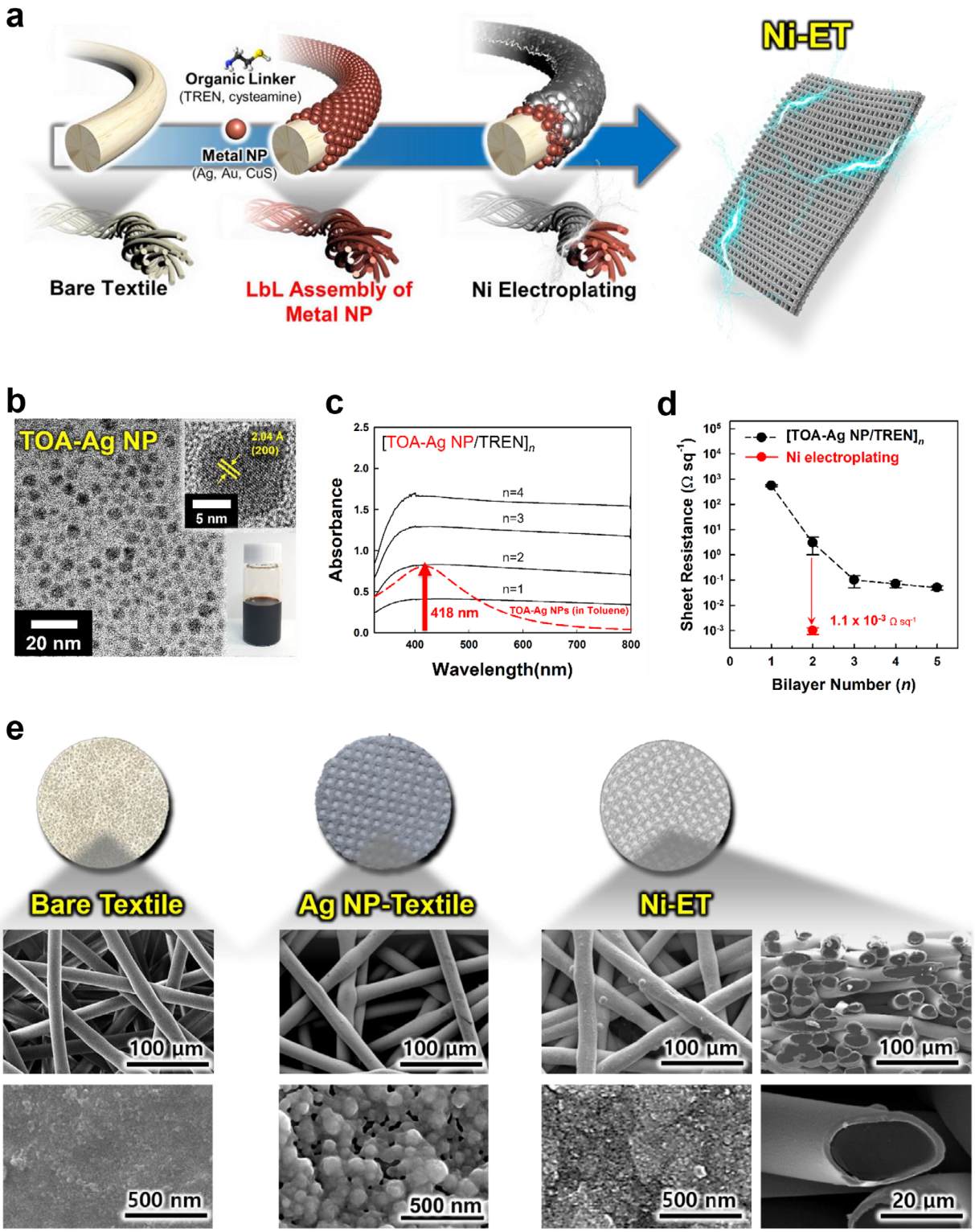

Figure 1. Preparation of Ni-ET. a) Schematic illustration for the preparation of Ni-electroplated textile. b) High-resolution transmission electron spectroscopy (HR-TEM) images of synthesized TOA-Ag NPs. The insets show the enlarged HR-TEM image of TOA-Ag NP with lattice fringes of 2.04 Å and a digital image of toluene solution containing TOA-Ag NP. c) UV–vis spectra of $[TOA\text{-}Ag\ NP/TREN]_n$ multilayers with different bilayer numbers (n). The red dashed line represents the characteristic surface plasmon resonance (SPR) peak at 418 nm for TOA-Ag NPs dispersed in toluene. d) Sheet resistance of the $(TOA\text{-}Ag\ NP/TREN)_n$-coated textile with different bilayer numbers (n) and the Ni-electroplated $[TOA\text{-}Ag\ NP/TREN]_2$-coated textile (i.e., Ni-ET). e) Digital images and field-emission scanning electron spectroscopy (FE-SEM) images of bare textile (left), $[TOA\text{-}Ag\ NP/TREN]_2$-coated textile (middle), and Ni-ET (right).

spectroscopy (XPS) (Figure S3, Supporting Information). Additionally, the formed Ni-ET maintained a highly porous structure of pristine polyester textile without any block-up phenomenon originating from metal NP aggregation and/or excessive Ni plating. Furthermore, it is important to note that TOA-CuS NPs and TOA-Au NPs, alongside TOA-Ag NPs, are also assembled using NH_2-functionalized molecular linkers such as TREN to produce conductive textiles with electrical conductivity that is well-suited for Ni electroplating (Figure S4, Supporting Information).

2.2. Ultrathin MOF-Coated LTA Using Coordination-Bonding LbL Assembly

Based on these results, we tried to deposit an ultrathin, lithiophilic MOF multilayer onto a highly porous Ni-ET. To accomplish this, Ag^+ ions in aqueous media (i.e., Ag_2CO_3-dissolved aqueous solution) were sequentially LbL-assembled with TCA in ethanol using complementary coordination bonding to form the Ag^+ ion-incorporated MOF multilayers, referred to as $[Ag^+/TCA]_n$-MOF multilayers (see **Figure 2a**). Specifically, the Ag^+ ions preferentially coordinate with the soft donor atoms (particularly sulfur) of deprotonated TCA molecules, primarily forming Ag-S coordination bonds (Figures S5 and S6, Supporting Information). Owing to the multiple coordination sites of TCA, each molecule can bridge several Ag^+ ions, facilitating the formation of an omnidirectional, crosslinked MOF network (Figure S7, Supporting Information). This LbL approach enables the in situ formation of an ultrathin and robust MOF architecture across the entire Ni-ET surface—a notable difference from previously reported MOF layers, which are primarily based on thick slurry pastes (at least several μm thickness) and often result in inadequate interfacial interactions.[47] With increasing the bilayer number (n) of $[Ag^+/TCA]_n$ multilayers, the absorbance peak intensity at 320 nm, originating from the triazine ring of TCA, increased progressively, as confirmed by UV–vis spectroscopy (Figure 2b). Correspondingly, the color of the Ni-ET changed visibly to gold, indicating a uniform and dense coating of the $[Ag^+/TCA]_n$ multilayers (see digital image in Figure 2b). We also quantitatively monitored the growth of multilayers using a quartz crystal microbalance (QCM). Figure 2c shows the frequency changes ($-\Delta F$) and corresponding mass changes of the adsorbed Ag^+ ions and TCA, resulting from an increasing layer number. The mass changes were calculated from the $-\Delta F$ values of the Ag ions and the TCA adsorbed on the crystal surface (Detailed Experimental Section, Supporting Information). Alternating the deposition of the Ag ions and the TCA resulted in $-\Delta F$ of 39.4 ± 5 (Δm of ≈697 ng cm^{-2}) per bilayer, respectively, indicating the layer-dependent vertical growth of multilayers. Given that our LbL technique allows for precise control over the thickness, composition, and uniformity of each component layer within the compact thin-film architecture, the surface area of the resulting porous $[Ag^+/TCA]_n$-coated Ni-ET (i.e., *n*-MOF-Ni-ET) is expected to increase systematically with the bilayer number (n). To validate this, we performed Brunauer–Emmett–Teller (BET) surface area analysis for $[Ag^+/TCA]_n$ multilayers with varying bilayer numbers (Figure S8, Supporting Information). The specific surface areas were measured to be 0.614, 1.263, 1.464, and 1.648 $m^2\ g^{-1}$ for $n = 0$, 1, 3, and 5, respectively, confirming that internal porosity and structural uniformity are well preserved throughout the CB-LbL assembly process. It is worth noting that our approach can be effectively applied to various metal atoms with distinct chemical characteristics, such as Cu and Co, enabling the optimal design tailored to specific functionality and performance requirements (Figure S9, Supporting Information).

The precise control over the deposition of each component through specific interfacial interactions enables a homogeneous distribution with a periodic configuration, potentially facilitating the formation of self-organized crystal lattices. As shown in Figure 2d, the LbL-assembled $[Ag^+/TCA]_3$-MOF multilayers exhibited high crystallinity, indicating a well-ordered framework structure. Specifically, the formed multilayers showed distinct diffraction peaks at 17.7, 22.6, 26.0, 32.7, and 38.2°, corresponding to the well-defined crystalline domains that result from the large periodicity of the MOF unit cell and the short-range coordination among its components.[48,49] This finding sharply contrasts with the results from composites produced through the simple blending between Ag^+ ions and TCA in solution. These structural characteristics of the $[Ag^+/TCA]_n$-MOF multilayers not only create a facile Li ion diffusion pathway with uniform current flux, but also effectively accommodate volume changes during Li plating/stripping processes. Additionally, the formed $[Ag^+/TCA]_n$-MOF multilayers exhibited the nanoporous surface morphology with the thickness of ≈8 nm per bilayer (Figure 2e; Figure S10, Supporting Information).

We also investigated the chemical properties of the LbL-assembled $[Ag^+/TCA]_n$-MOF multilayers using XPS analysis. As shown in Figure 2f, the multilayers primarily exhibit the Ag^+ state, with no detectable presence of metallic Ag^0. Additionally, the TCA in the $[Ag^+/TCA]_n$-MOF multilayers manifests in two different chemical forms, attributed to the resonance structure of the triazine ring (Figure 2g). That is, the deconvolution of N 1s spectrum displayed peaks at 398 and 400.4 eV, corresponding to C═N—C and N—C bonds, respectively. Notably, the enhanced intensity of the C═N—C peak in the multilayers, compared to TCA alone (Figure S11, Supporting Information), suggests polymerization between Ag and TCA, confirming the development of a polymerized MOF structure.

2.3. Characterization of $[Ag^+/TCA]_n$-MOF Multilayers on Li Deposition

Electrolyte wettability of the anode surface is a crucial factor affecting the electrochemical performance, ion transport behavior, and interfacial stability of the battery systems. The organic linkers (TCA) within the $[Ag^+/TCA]_n$-MOF multilayers exhibit the hydrophilic properties due to the presence of abundant polar functional groups, such as thiol and amide, enabling the superior electrolyte wettability compared to that of a bare Ni plate (Figure S12, Supporting Information). It is noteworthy that the Ni plate demonstrated complete wettability with the electrolyte (1 M LiTFSI in 1,3-Dioxolane/Dimethoxyethane (DOL/DME, 1:1 vol%) with 5 wt.% $LiNO_3$) after the deposition of $[Ag^+/TCA]_3$ multilayers, indicating high coating quality. These characteristics suggest the possibility that the $[Ag^+/TCA]_n$-MOF multilayers can induce the uniform electrolyte distribution across the accessible electrode surface of 3D-structured Ni-ETs, facilitating ion

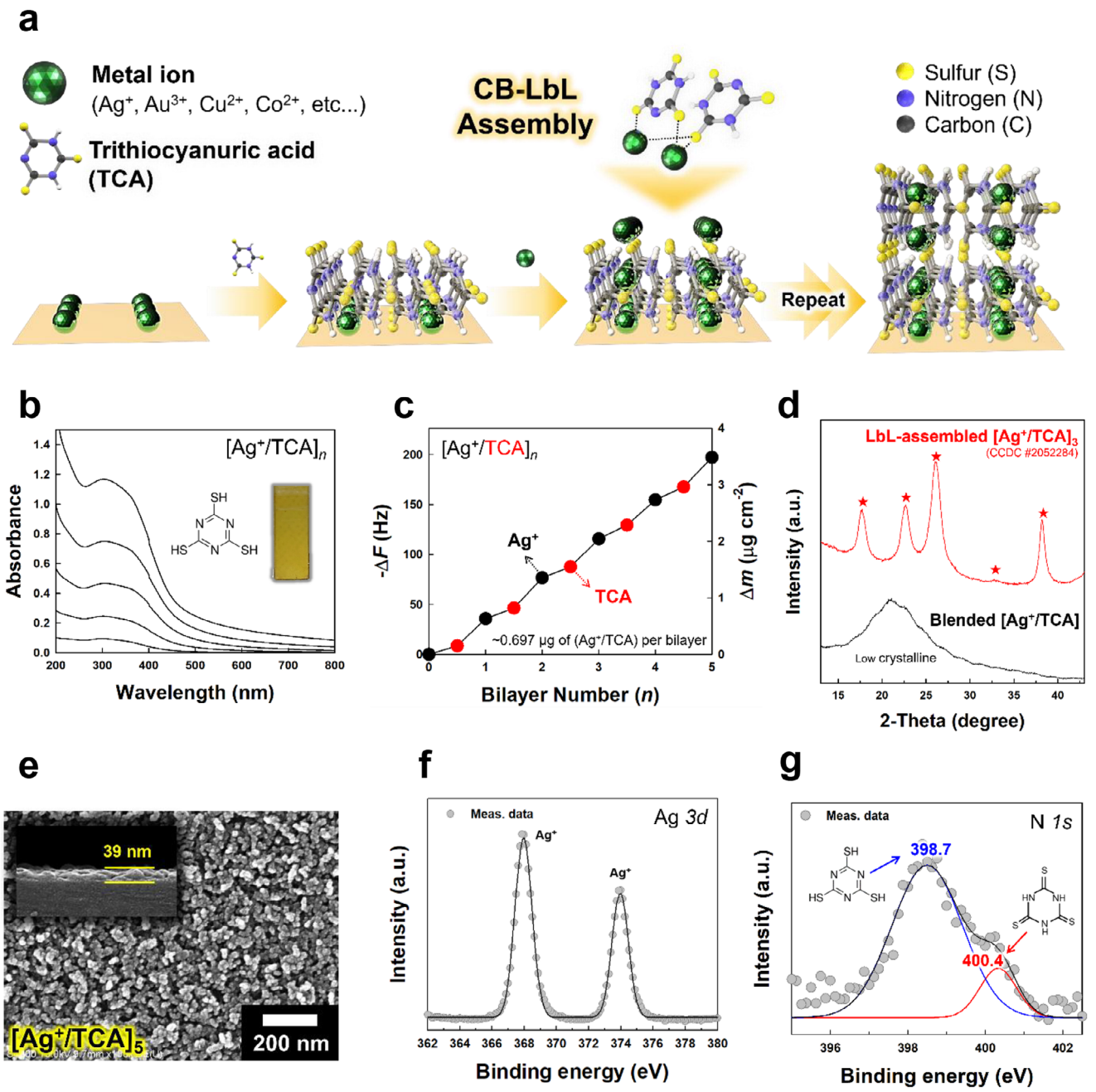

Figure 2. LbL-assembled MOF multilayers. a) Schematic illustration for the preparation of LbL-assembled $[Ag^+/TCA]_n$ multilayers onto Ni-ET. b) UV–vis spectra and c) QCM data of $[Ag^+/TCA]_n$ multilayers with different bilayer numbers (n). Insets in Figure 2b show the molecular structure of TCA and a digital image of $[Ag^+/TCA]_n$ multilayer-coated quartz substrate. d) XRD patterns of LbL-assembled $[Ag^+/TCA]_3$ multilayers and blended Ag^+-TCA films. e) FE-SEM image of $[Ag^+/TCA]_5$ multilayers onto Si wafer. The inset shows the cross-sectional FE-SEM image of $[Ag^+/TCA]_5$ multilayers. f) Ag 3d and g) N 1s XPS spectra of $[Ag^+/TCA]_5$-MOF multilayers. Deconvolution of the N 1s spectrum reveals the presence of two types of molecular structures of TCA within the $[Ag^+/TCA]_5$-MOF multilayers.

diffusion and lowering the energy barrier for the Li nucleation process.

For confirming this possibility, the $[Ag^+/TCA]_n$-MOF multilayers were coated onto the Ni-ET current collectors using the aforementioned CB-LbL assembly, followed by sequential Li electroplating at 6 mAh cm^{-2} in 1 M LiTFSI in DOL/DME mixture (**Figure** 3a). Figure 3b compares the potential difference of the n-MOF-Ni-ET and the bare Ni-ET on Li plating at a current density of 0.1 mA cm^{-}[2] and an areal capacity of 6 mAh cm^{-2}. In contrast to the bare Ni-ET with a nucleation overpotential of 19.3 mV, the n-MOF-Ni-ETs demonstrated significantly reduced values of 8.1, 3.9, and 1.6 mV for n = 1, 3, and 5, respectively. These observations suggest that an increase in the amount of hydrophilic (or lithiophilic) moieties within the $[Ag^+/TCA]_n$-MOF

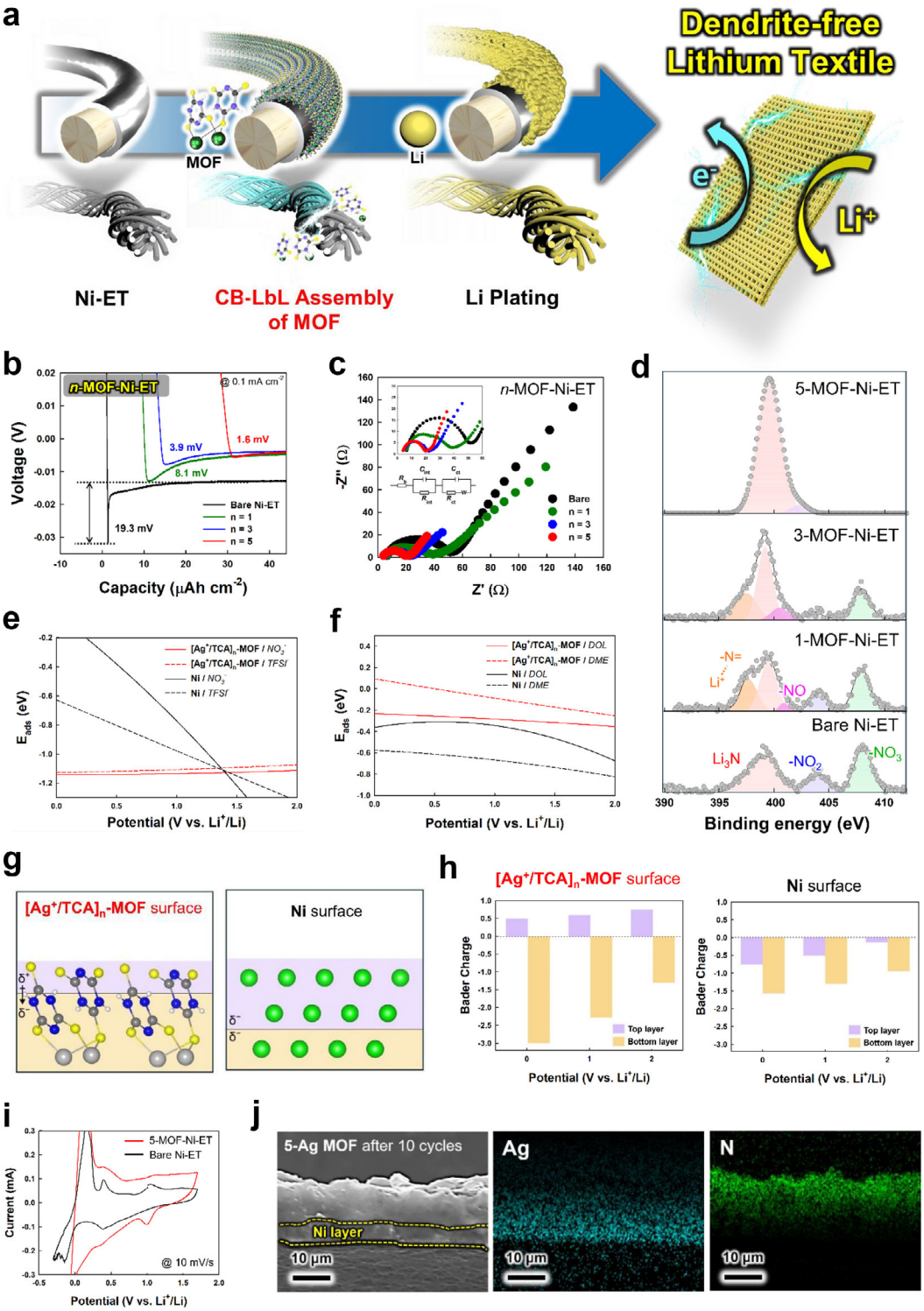

Figure 3. Li textile anode. a) Schematic illustration for the preparation of LTA. b) Voltage (V) versus capacity (μAh cm^{-2}) curves of bare Ni-ET and *n*-MOF-Ni-ET-based half-cells during Li nucleation at 0.1 mA cm^{-2} and 6 mAh cm^{-2}. b) Nyquist plots of bare Ni-ET and *n*-MOF-Ni-ET half-cells. Insets show enlarged impedance curves in the high-frequency region and the representative equivalent circuit. d) N 1s XPS spectra of bare Ni-ET and *n*-MOF-Ni-ETs with different bilayer numbers (*n*). Calculated anion adsorption energy (E_{ads}) versus potential curves of e) anion molecules (NO_3^- and $TFSI^-$) and f) solvent molecules (DME and DOL) adsorbed onto bare Ni-ET and *n*-MOF-Ni-ET electrodes. g) Schematic illustration of surface configurations for bare Ni-ET and *n*-MOF-Ni-ET surfaces. h) Bader charge analysis of bare Ni and $[Ag^+/TCA]_5$-MOF surfaces at different potentials. i) Cyclic voltammograms of bare Ni-ET and 5-MOF-Ni-ET electrodes at a scan rate of 10 mV s^{-1}. j) Cross-sectional FE-SEM image and corresponding elemental mapping images (Ag and N) of the 5-MOF-Ni-ET electrode after 10 cycles.

multilayers enhances nucleation efficiency by reducing the ion concentration gradient at the interface. Consequently, the hydrophilic properties of $[Ag^+/TCA]_n$-MOF multilayers not only diminish unnecessary energy loss during battery operations but also potentially suppress the formation of Li dendrites, which are typically caused by localized current density. Additionally, electrochemical impedance spectroscopy (EIS) analysis revealed a consistent decrease in charge transfer resistance (R_{ct}) with increasing bilayer number (*n*) in the *n*-MOF-Ni-ET samples (Figure 3c). This trend indicates that the $[Ag^+/TCA]_n$-MOF multilayers facilitate more efficient Li^+ ion transport to the electrode surface. As a result, high-quality, conformal Li coatings were achieved while the highly porous architecture of the textile substrate was impeccably preserved (Figure S13, Supporting Information). In contrast, Li plating on the bare Ni-ET resulted in nonuniform and agglomerated Li deposition, which obstructed the porous structure of the textile substrate (Figure S14, Supporting Information). As a result, the *n*-MOF-coated Ni-ETs (or *n*-MOF-coated LTAs), which exhibit both highly macroporous (inherent to the pristine textile) and nanoporous structure (contributed by the MOF multilayers) structures, were successfully prepared through a CB-LbL assembly.

The formation of a stable SEI layer on the anode surface is critical for cell performance, which is strongly influenced by surface charge density and SEI composition. The SEI is formed by the decomposition of electrolyte components adsorbed onto the electrode's inner Helmholtz plane (IHP). At typical electrode interfaces, only a limited number of anions initially occupy the IHP. When an external current is applied, these anions are displaced from the IHP due to electrostatic repulsion, resulting primarily in the reduction of free solvent molecules. This preferential solvent reduction produces an SEI layer deficient in critical inorganic components such as Li_3N and LiF, thus exhibiting weak mechanical strength and limited chemical stability. However, the introduction of $[Ag^+/TCA]_n$-MOF generates strong surface dipoles at the IHP, significantly enhancing the adsorption forces acting upon the anions. Consequently, these anions remain anchored to the IHP even under electrostatic repulsion during charging, facilitating the formation of an anion-derived SEI that demonstrates superior chemical stability and enhanced mechanical robustness. Moreover, the complete conversion of $LiNO_3$ to Li_3N at the electrode/electrolyte interface during electrochemical operation faces a high energy barrier due to the strong N—O bonds in the NO_3^- anion, which necessitates multielectron transfer processes.[50] In this regard, the nitrogen groups (—N=) in the triazine ring structure of TCA facilitate electron transfer to $LiNO_3$, thereby promoting its decomposition into Li_3N and lithium oxides, which subsequently contribute to the formation of the SEI layers.[51–53] As evidenced in the deconvoluted N 1s XPS spectra after the 10th CV sweeps (Figure 3d), the bare Ni-ET electrodes displayed characteristic peaks for Li_3N and its intermediates (LiN_xO_y), whereas the $[Ag^+/TCA]_n$-MOF-coated LTAs showed a gradual decrease in the peak intensities of intermediates. Notably, the 5-MOF-coated LTAs exhibited a more pronounced single Li_3N peak. This observation indicates that the $[Ag^+/TCA]_n$-MOF multilayers facilitate the complete decomposition of $LiNO_3$ into Li_3N, through dipole-dipole interactions within the inner Helmholtz plane. In particular, increasing the bilayer number (n) of $[Ag^+/TCA]_n$-MOF multilayers leads to a higher density of TCA molecules—rich in nitrogen groups—which effectively lowers the energy barrier for this phase transformation. A similar trend was observed in TCA-based electrodes without the Ag NP component, clearly confirming the pivotal role of TCA in facilitating the formation of Li_3N-rich SEI (Figure S15, Supporting Information). Additionally, the polarized surface of the $[Ag^+/TCA]_n$-MOF multilayers during discharge generates localized electric dipoles that can interact with $TFSI^-$ anions in the inner Helmholtz plane, thereby facilitating their reduction to LiF (Figure S16, Supporting Information).

To gain deeper insight into the influence of surface dipole moments, we performed density functional theory (DFT) calculations. However, conventional DFT simulations are inherently limited in capturing the effects of applied electrochemical potentials, as they are typically conducted under constant-charge conditions with a fixed total number of electrons. To overcome this limitation and better approximate experimental conditions, we employed the grand-canonical DFT (GC-DFT) framework. Unlike traditional methods, GC-DFT enables simulations under constant-potential conditions by dynamically adjusting the electron count in the system to match a specified target potential.

Using the GC-DFT approach, we calculated the adsorption energies of various molecules adsorbed on electrode surfaces across different applied potentials. Specifically, we compared two surface models: a bare Ni surface and a $[Ag^+/TCA]_n$-MOF surface. To examine the interactions between solvent molecules and these surfaces, we investigated the adsorption energies of various solvent molecules (i.e., DME and DOL) and anion molecules (i.e., NO_3^-, and $TFSI^-$). The atomic structures of these solvent molecules are shown in Figure S17 (Supporting Information). On the bare Ni surface, anion adsorption energies increased as the potential decreased from 2 to 0 V, indicating stronger adsorption at lower potentials (Figure 3e). In contrast, the $[Ag^+/TCA]_n$-MOF surface exhibited the opposite trend, with anion adsorption energies decreasing as the potential decreased. These results indicate that anions are more stably adsorbed on the MOF-modified Ni surface than on bare Ni at low potentials.

For the solvent molecules, the adsorption energies were consistently lower on the Ni surface compared to the $[Ag^+/TCA]_n$-MOF surface across the full potential range (0–2 V), implying that ether molecules (in DOL/DME) are more stable on the Ni surface (Figure 3f). We attribute the enhanced anion adsorption on the $[Ag^+/TCA]_n$-MOF surface to the presence of TCA molecules, which induce a strong surface dipole moment. This dipole arises from a positively charged top layer and negatively charged underlying layers, generating a strong Coulombic attraction toward anions. In contrast, the bare Ni surface exhibits only a weak dipole, with relatively less negative charge in the upper layers compared to the bottom, resulting in reduced anion affinity.

To further validate the role of surface dipole moments and surface charges, we performed Bader charge analysis at potentials of 0, 1, and 2 V, focusing on the top two atomic layers and the underlying layers of both surfaces (Figure 3g; Figure S18, Supporting Information). On the bare Ni surface, all layers displayed negative charges at every potential, with the degree of negativity increasing as the potential decreased (Figure 3h). This growing surface negativity at lower potentials likely contributes to the reduced anion adsorption, as stronger electrostatic repulsion hinders anion approach and binding. In contrast, Bader charge analysis revealed

that $[Ag^+/TCA]_n$-MOF surface displayed a positively charged top layer and negatively charged lower layers, confirming the formation of a significant surface dipole. Furthermore, as the applied potential decreased, the charge separation between the positively charged upper layer and the negatively charged lower layers became more pronounced (Figure 3g,h). This enhancement in the surface dipole moment effectively mitigates the electrostatic repulsion associated with the applied potential, thereby promoting stable anion adsorption on the $[Ag^+/TCA]_n$-MOF surface.

This phenomenon was further confirmed by cyclic voltammetry (CV) measurements conducted on the 5-MOF-Ni-ETs and bare Ni-ET electrodes at a scan rate of 10 mV s^{-1} (Figure 3i). During the cathodic sweep, the 5-MOF-Ni-ETs exhibited significantly higher current responses compared to the bare Ni-ET electrodes in the potential range of 0.9 to 1.2 V (vs Li^+/Li). The observed reduction peak at ≈1.0 V is associated with the reduction of NO_3^- and $TFSI^-$ anions, which are essential for SEI formation, implying that the $[Ag^+/TCA]_n$-MOF multilayers effectively retain a large number of anion molecules (i.e., NO_3^- and $TFSI^-$) at the interface.[51–53] In addition, the LbL-assembled $[Ag^+/TCA]_n$-MOF multilayers on the Ni-ET current collector retained their structural integrity even after repeated Li plating/stripping cycles, despite the considerable volume changes involved in these processes, which was confirmed by cross-sectional FE-SEM images and energy dispersive X-ray spectroscopy (EDS) mapping images (Figure 3j; Figure S19, Supporting Information). Furthermore, during cathodic sweeps in the low potential range (typically below 1 V), the electrons transferred from the electrode reduce Ag^+ ions in the MOF multilayer to metallic Ag^0 (370.1 and 376.1 eV), forming lithiophilic Ag NPs along with the Ag-Li alloy phases (368.5 and 374.5 eV) (Figure S20, Supporting information). After the Li stripping step, Li was extracted from the electrode, leaving only metallic Ag^0 peaks, indicating reversible alloying/dealloying behavior that remained consistent over repeated cycles. This behavior enables the in situ formation of a well-distributed, ultrathin layer of lithiophilic Ag NPs without requiring additional chemical treatments (Figures S21 and S22, Supporting Information). As a result, structural deformation is minimized, preserving electrochemical stability throughout cycling. Notably, in the case of 5-MOF-Ni-ET, the reduction of Ag^+ ions was completed immediately after the first Li plating/stripping cycle, demonstrating highly efficient and rapid electron transfer across the uniformly assembled MOF multilayers.

2.4. Electrochemical Properties in Half-Cell and Symmetric Cell Configurations

To evaluate the effect of *n*-MOF-Ni-ETs on the formation of the SEI layer, we examined electrochemical properties using a half-cell configuration (i.e., Li//Li-*n*-MOF-Ni-ET). As a first step, the Li-ion diffusion behavior within the electrode was analyzed using EIS measurements during successive Li plating/stripping cycles (**Figure 4a**; Figure S23, Supporting Information). In LMB systems, the diffusion coefficient (D), which quantifies the rate at which charged species migrate through the electrolyte, plays a critical role in the dynamic formation and growth of the SEI layer. Variations in diffusion coefficients can influence Li-ion transport by altering interfacial resistance and modifying ionic conduction pathways. Based on the parameters obtained from the Nyquist plots after 10 CV cycles, the diffusion coefficients for each cell were calculated using the following equations:[54]

$$Z' = R_s + R_{ct} + \sigma_w \omega^{-0.5} \tag{1}$$

$$D = 0.5 \left(\frac{RT}{AF^2 \sigma_w C} \right)^2 \tag{2}$$

where $\sigma_w$is the Warburg impedance coefficient, ω is the angular frequency, R is the gas constant, T is the absolute temperature (K), A is the electrode area (cm^2), F is Faraday's constant (C mol^{-1}), and C is the molar concentration of ions in the electrolyte (mol L^{-1}).

As shown in Figure 4b, the ion diffusion coefficient values of Li-*n*-MOF-Ni-ETs were determined to be 1.02×10^{-12}, 3.06×10^{-12}, 41.8×10^{-12}, and 67.3×10^{-12} cm^2 s^{-1} for $n = 0$ (bare Ni-ET), 1, 3, and 5, respectively. Notably, a sharp increase in diffusion coefficient was observed at $n = 3$, indicating a threshold beyond which the presence of $[Ag^+/TCA]_n$-MOF multilayers significantly enhances ion transport. This behavior is likely attributed to the formation of a sufficient quantity of $[Ag^+/TCA]_n$-MOF multilayers at $n \geq 3$, which not only improves ion diffusion but also promotes the development of Li_3N within an anion-rich SEI layer—an interpretation consistent with the XPS results shown in Figure 3d. Additionally, the R_{SEI} values gradually decreased with increasing the bilayer number (n) of Li-*n*-MOF-Ni-ETs, further supporting the formation of a high-quality, Li_3N-rich SEI layer with improved ionic conductivity (Figure 4c). However, when the bilayer number (n) was further increased to 10, a slight rise in charge transfer resistance (R_{ct}) was observed, likely due to the additional resistance induced by the increased thickness of the MOF film. Importantly, the Li-5-MOF-Ni-ET exhibited the highest Li^+ transference number of 0.67, indicating superior ion transport efficiency and stable electrochemical performance (Figure 4d).

The CE value during continuous electrochemical cycling reflects the operational reversibility of the battery cells, which is closely related to the quality of the SEI layer. As shown in Figure 4e, the CE values were recorded for each cell under galvanostatic charge-discharge (GCD) cycling at 1 and 1 mAh cm^{-2}. The relatively low CE values during the initial cycles are primarily attributed to the formation of the SEI layer, which irreversibly consumes a portion of Li ions at the anode surface (Figure S24, Supporting Information). Among the tested electrodes, the Li-5-MOF-Ni-ET exhibited a noticeably higher CE value during the early GCD cycles compared to the others, indicating that the SEI formation occurs more efficiently with reduced irreversible Li loss. This behavior implies the rapid formation of a stable, thinner, and more ion-conductive SEI layer on the Li-5-MOF-Ni-ET, which in turn enables excellent cycling reversibility (Figure S25, Supporting Information). The formation of this high-quality SEI also promotes smoother and denser lithium plating, in stark contrast to the bare Ni-ET, which exhibits nonuniform, needle-like lithium growth (Figure S26, Supporting Information). As a result, the (Li//Li-5-MOF-Ni-ET) half-cells demonstrated superior operational stability, achieving a CE of

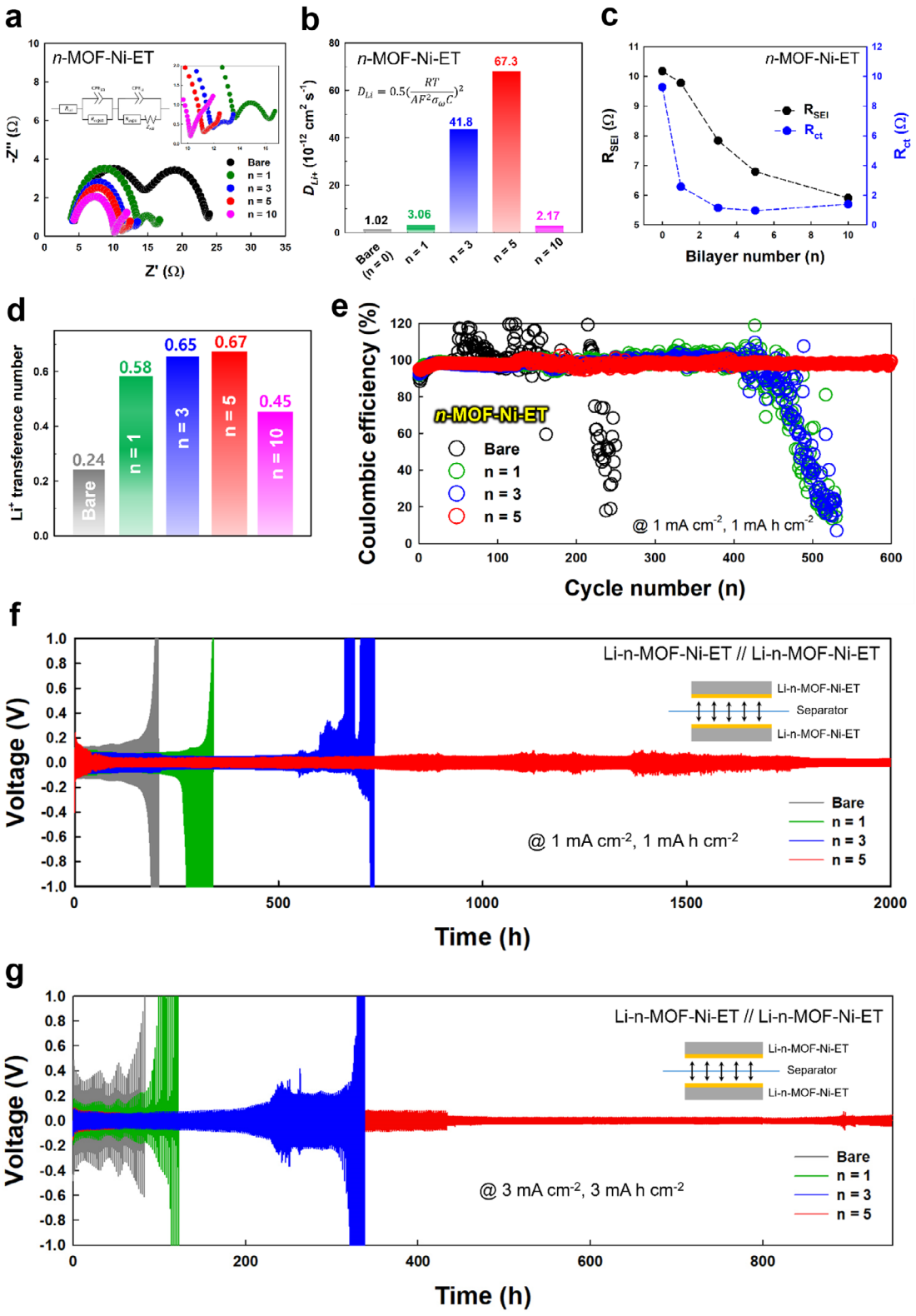

Figure 4. Symmetric cell tests. a) Nyquist plots of Li//Li-*n*-MOF-Ni-ET half-cells as a function of bilayer number (*n*) of 0, 1, 3, and 5. Insets show enlarged impedance spectra in the low-frequency region and the representative equivalent circuit. b) Ion diffusion coefficients ($D_{Li}{}^+$), and c) R_{SEI} and R_{ct} values of Li//Li-*n*-MOF-Ni-ET half-cells as a function of bilayer number (*n*). d) Li^+ transference number of Li//Li-*n*-MOF-Ni-ET half-cells as a function of bilayer number (*n*). e) CE values of Li//Li-*n*-MOF-Ni-ET half-cells during Li plating/stripping cycles at 1 mA cm^{-2} and 1 mAh cm^{-2}. Galvanostatic cycling of bare Ni-ET and *n*-MOF-Ni-ET-based symmetrical full-cells at f) 1 mA cm^{-2} (1 mAh cm^{-2}) and g) 3 mA cm^{-2} (3 mAh cm^{-2}).

≈99.7% over 600 cycles, outperforming other cell configurations (Figure 4e).

The cycle retention performance of the Li-*n*-MOF-Ni-ETs was further evaluated using a symmetrical full-cell configuration (i.e., Li-*n*-MOF-Ni-ET//Li-*n*-MOF-Ni-ET) under two different operating conditions: 1 mA cm^{-2}/1 mAh cm^{-2} and 3 mA cm^{-2}/3 mAh cm^{-2} (Figure 4f,g). Under these conditions, the bare Ni-ETs showed significant fluctuations in CE values after only 50 cycles. In contrast, the Li-n-MOF-Ni-ETs maintained excellent stability, sustaining CE values close to 100% for over 400 cycles. In particular, the Li-5-MOF-Ni-ET-based cells demonstrated outstanding long-term performance, retaining stable operation for 2000 h (1000 cycles) at 1 mA cm^{-2} (1 mAh cm^{-2}), and for 950 h (475 cycles) at 3 mA cm^{-2} (3 mAh cm^{-2}), with smooth and consistent voltage profiles. In this case, the small decreases or slight fluctuations in overpotential observed during the cycling of Li-5-MOF-Ni-ET-based symmetric cells—particularly in the absence of signs of severe cell degradation—are likely attributable to benign factors such as minor interfacial rearrangements, thermal fluctuations, or electrode surface activation (Figure S27, Supporting Information). Importantly, the excellent cycling stability of the Li-5-MOF-Ni-ET-based cells is primarily attributed to the formation of a high-quality solid electrolyte interphase (SEI) enriched with inorganic components such as Li_3N and LiF, which collectively contribute to superior mechanical robustness and high ionic conductivity.

To validate this hypothesis, we performed both nanoindentation and real-time electrochemical impedance spectroscopy (EIS) analyses on SEI layers formed on electrodes with and without the Li-*n*-MOF after prolonged cycling. The SEI formed on the Li-5-MOF-Ni electrode exhibited significantly higher mechanical hardness (0.31 GPa) than that on the bare Ni electrode (0.03 GPa), indicating markedly improved mechanical stability (Figure S28, Supporting Information). This enhancement is likely due to the formation of a Li_3N-rich SEI. Furthermore, analysis of the force–indentation curves revealed that the SEI thickness on the Li-5-MOF-Ni electrode was ≈137 nm, compared to 346 nm on the bare Ni electrode, suggesting that the MOF promotes the formation of a thinner, denser, and more compact interfacial layer on the lithium metal surface.

Consistent with these mechanical findings, Nyquist plots (Figure S29, Supporting Information) show that the Li_3N-rich SEI on the Li-5-MOF-Ni-ET electrode maintains a smaller and more stable high-frequency semicircle throughout 100 cycles, corresponding to a reduced and nearly constant SEI resistance (R_SEI). In contrast, the SEI on the bare Ni-ET electrode shows a gradual increase in semicircle diameter, indicating a continuous rise in R_SEI and ongoing interfacial restructuring. These results collectively suggest that the Li_3N-rich SEI not only provides enhanced mechanical durability but also sustains excellent ionic conductivity, likely owing to the intrinsically fast Li^+ transport pathways within Li_3N. Therefore, these results clearly demonstrate that the LbL-assembled ultrathin MOF multilayers effectively regulate Li deposition behavior and SEI formation. Moreover, they highlight that electrochemical performance can be finely tuned through simple and precise control over the number of MOF bilayers.

2.5. Electrochemical Performance of $LiFePO_4$-Based Full Cell

To more accurately assess the practical performance of the Li-*n*-MOF-Ni-ET anodes, asymmetrical full-cells were designed using a $LiFePO_4$ (LFP) cathode with a mass loading of 3 mg cm^{-2} and tested under GCD cycling at 1C within a voltage range of 2.5–3.9 V (**Figure 5a**). In stark contrast to the bare Ni-ET, which exhibited poor capacity retention of less than 200 cycles, the Li-5-MOF-Ni-ET anode maintained ≈96.5% of its initial capacity (0.441 mAh cm^{-2}) over 1300 cycles, demonstrating outstanding long-term stability. Furthermore, when paired with a high loading LFP cathode (16.7 mg cm^{-2}) to achieve an N/P ratio of 1.4, the Li-5-MOF-Ni-ET anode delivered a reversible capacity of 2.26 mAh cm^{-2} (≈92% retention) and a CE of 99.8% after 180 cycles (Figure 5b; Figure S30, Supporting Information), indicating efficient ion transport and stable SEI formation. Notably, the (Li-5-MOF-Ni-ET//LFP) full-cell (N/P = 1.4) exhibited excellent rate performance, delivering a capacity of ≈1.81 mAh cm^{-2} (106.5 mAh g^{-1}) even at a high rate of 5 C. Upon returning to 1 C, the capacity fully recovered to 2.44 mAh cm^{-2} (144 mAh g^{-1}), highlighting the superior mass transport and charge conduction capabilities provided by the LbL-assembled MOF structure (Figure 5c). As a result, the full cells utilizing the Li-5-MOF-Ni-ET anode achieved maximum energy and power densities of 9.14 mWh cm^{-2} and 48.3 mW cm^{-2}, respectively, based on the area of the cell (Figure 5d). These values significantly surpass those reported for LFP full cells using previously developed Li-deposited anode as well as those employing Li foils (inset of Figure 5d)

To further expand the applicability of the Li-5-MOF-Ni-ET, 10.5 mAh-level pouch cells were fabricated using an LFP cathode with a high areal capacity of 3.5 mAh cm^{-2} (N/P ratio ≈1.1), and their electrochemical performance was investigated. Notably, the 3−MWCF separator-based pouch cells achieved an outstanding capacity retention of 98.6% per cycle for 100 cycles (Figure 5e; Figure S31, Supporting Information). These results clearly demonstrate that our MOF multilayer–assembled LTA enables precise control over lithium dendrite growth through its tailored functionality and structural design, thereby significantly improving overall cell performance. Although the current demonstration serves as a proof-of-concept using a small-scale system (10.5 mAh), our approach holds strong potential for scaling up to large-area pouch cells. This is because the solution-based LbL assembly process can be readily applied to a wide range of substrates, regardless of their size or geometry (Figure S32, Supporting Information). Therefore, our method is well-suited for the scalable fabrication of electrodes and enables the uniform deposition of active components even on substrates with complex 3D structures, such as textiles.

3. Conclusion

In summary, we have successfully developed a high-performance LTA that enables LMBs with both high capacity and long-term cycling stability. This achievement was made possible through the precise and uniform deposition of ultrathin lithiophilic MOF multilayers onto a highly porous textile current collector. These multilayers were fabricated via a repeated CB-LbL assembly of Ag^+ ions and the TCA organic linker, without the need for any

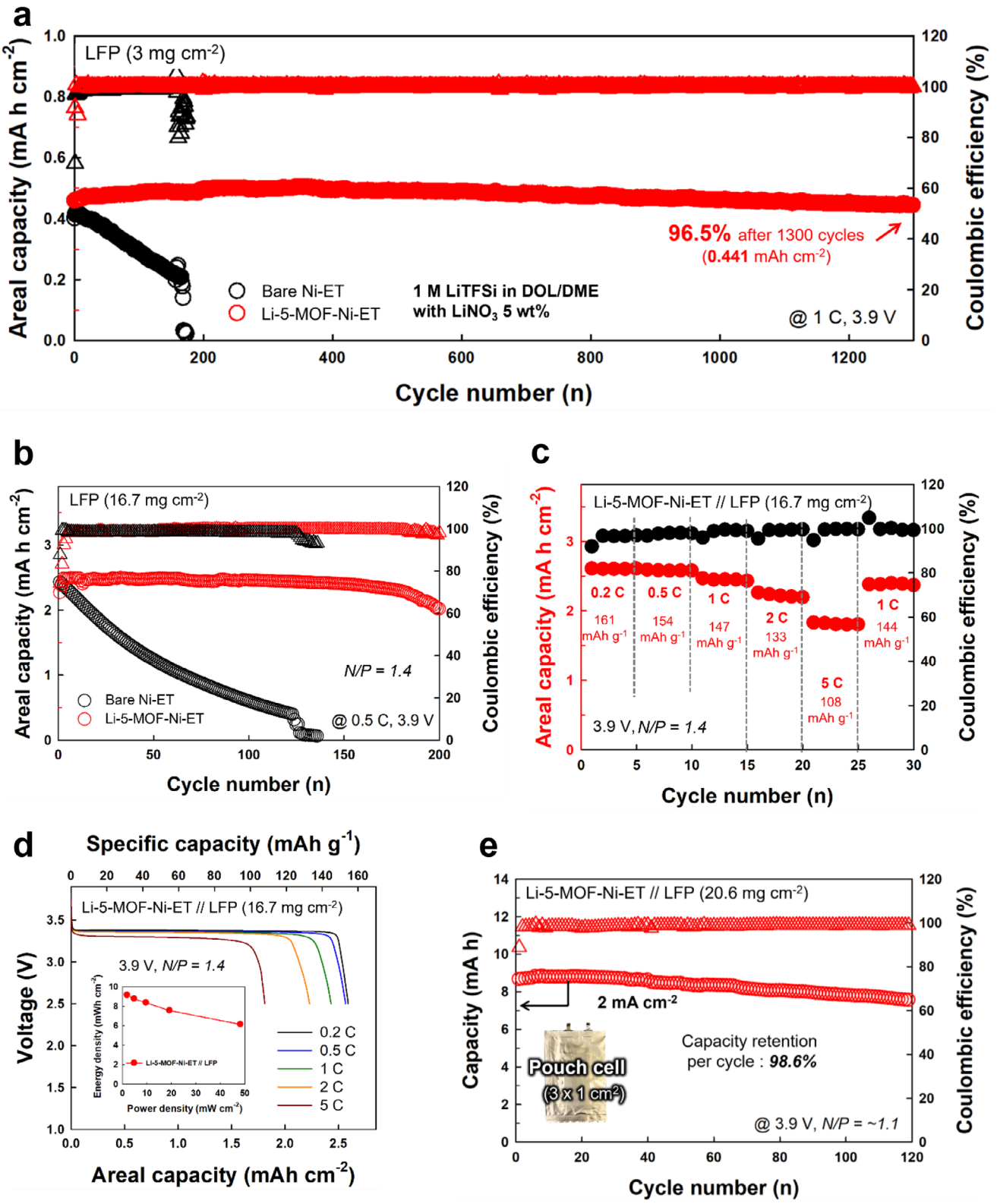

Figure 5. Performance of asymmetric full-cell. Cycling tests of Li-5-MOF-Ni-ET//LFP and bare Ni-ET//LFP full-cells at cathode loading of a) 3 mg cm^{-2} and b) 16.7 mg cm^{-2}. c) Rate-capability and CE values of Li-5-MOF-Ni-ET//LFP. d) Current density-dependent discharge profiles of Ni-ET//LFP full-cells with a cathode loading of 16.7 mg cm^{-2}. The inset presents the energy and power densities at varying current densities. e) Capacity retention of Li-5-MOF-Ni-ET//LFP pouch cells with a cathode loading of 20.6 mg cm^{-2}, tested at 2 mA cm^{-2} (N/P ratio ≈1.1). The inset shows a digital image of the assembled pouch cell.

additional complex synthesis steps. During electrochemical cycling, the $[Ag^+/TCA]_n$-MOF multilayers underwent in situ chemical reduction to form lithiophilic Ag NPs, which effectively lowered the lithium nucleation barrier. In addition, the TCA linkers within the MOF contributed to the formation of an anion-rich SEI layer, particularly enriched with Li_3N compounds. This multifunctional role of the $[Ag^+/TCA]_n$-MOF multilayers—facilitating uniform lithium plating at the electrode interface while catalyzing the formation of a thin, dense, and highly ion-conductive SEI layer—represents a significant advancement over previous approaches, such as MOF-based strategies primarily focused on separator modification, and lithiophilic metal NP-based methods aimed at interlayer coatings on host materials. The optimized Li-5-MOF-Ni-ET anode achieved a CE of 99.1% after 600 cycles at 1 mA cm^{-2}/1 mAh cm^{-2}. In symmetric cell configurations, it exhibited remarkable cycling stability, operating continuously for over 2000 h under the same conditions. Furthermore, when paired with an LFP cathode in a full cell, the system maintained 96.5% capacity retention over 1300 cycles and demonstrated excellent electrochemical performance in a pouch cell format. These findings underscore the potential of our CB-LbL-assembled ultrathin, lithiophilic MOF-based LTA to drive the development of next-generation, dendrite-free, high-performance LMBs.

Supporting Information

Supporting Information is available from the Wiley Online Library or from the author.

Acknowledgements

This work was supported by National Research Foundation of Korea (NRF) grant funded by the Korean government (Ministry of Science and ICT) (Grant No. 2021R1A2C3004151, RS-2024-00451691, RS-2025-02214734, RS-2025-25413074), and DGIST R&D Programs of the Ministry of Science and ICT of Korea (25-ET-01). The authors also acknowledge support from KIST International Program (2V09840-23-P025) and the KU-KIST Graduate School of Converging Science and Technology Program. S.B. acknowledges the support from the Nano & Material Technology Development Program through the National Research Foundation of Korea(NRF) funded by the Ministry of Science and ICT (RS-2024-00448287) and generous supercomputing time from KISTI.

Conflict of Interest

The authors declare no conflict of interest.

Author Contributions

D.N. and G.Y. contributed equally to this work. D.N., S.B., S.W.L., Y.K., and J.C. conceived and designed the experiments. D.N. and G.Y. conducted experiments and data analysis. C.L., J.A., B.K., S. C., K.H.K., D.R., H.K., J.G.S., H.J.K., and J.L. assisted the experimental process. D.N., G.Y., S.B., S.W.L., Y.K., and J.C. co-wrote the manuscript. All authors analyzed the results and commented on the manuscript.

Data Availability Statement

The data that support the findings of this study are available from the corresponding author upon reasonable request.

Keywords

coordination-bonding layer-by-layer assembly, Li textile anode, MOF multilayers

Received: April 30, 2025
Revised: August 8, 2025
Published online: September 13, 2025

[1] W. Xu, J. Wang, F. Ding, X. Chen, E. Nasybulin, Y. Zhang, J.-G. Zhang, *Energy Environ. Sci.* **2014**, *7*, 513.
[2] J. Liu, Z. Bao, Y. Cui, E. J. Dufek, J. B. Goodenough, P. Khalifah, Q. Li, B. Y. Liaw, P. Liu, A. Manthiram, Y. S. Meng, V. R. Subramanian, M. F. Toney, V. V. Viswanathan, M. S. Whittingham, J. Xiao, W. Xu, J. Yang, X.-Q. Yang, J.-G. Zhang, *Nat. Energy* **2019**, *4*, 180.
[3] S. Tan, Z. Shadike, X. Cai, R. Lin, A. Kludze, O. Borodin, B. L. Lucht, C. Wang, E. Hu, K. Xu, X.-Q. Yang, *Electrochem. Energy Rev.* **2023**, *6*, 35.
[4] E. Cha, M. D. Patel, J. Park, J. Hwang, V. Prasad, K. Cho, W. Choi, *Nat. Nanotechnol.* **2018**, *13*, 337.
[5] K. Chen, D.-Y. Yang, G. Huang, X.-B. Zhang, *Acc. Chem. Res.* **2021**, *54*, 632.
[6] W. Wu, W. Luo, Y. Huang, *Chem. Soc. Rev.* **2023**, *52*, 2553.
[7] H. Dai, X. Gu, J. Dong, C. Wang, C. Lai, S. Sun, *Nat. Commun.* **2020**, *11*, 643.
[8] Y. Zhang, Y. Wu, H. Li, J. Chen, D. Lei, C. Wang, *Nat. Commun.* **2022**, *13*, 1297.
[9] K. Ryu, K. Lee, J. Lim, M. J. Lee, K.-H. Kim, U. H. Lee, B. L. D. Rinkel, K. Kim, S. Kim, D. Kim, D. Shin, B. McCloskey, J. Kang, S. W. Lee, *Energy Environ. Sci.* **2024**, *17*, 7772.
[10] Y. Liu, R. Hu, D. Zhang, J. Liu, F. Liu, J. Cui, Z. Lin, J. Wu, M. Zhu, *Adv. Mater.* **2021**, *33*, 2004711.
[11] F. Zhao, P. Zhai, Y. Wei, Z. Yang, Q. Chen, J. Zuo, X. Gu, Y. Gong, *Adv. Sci.* **2022**, *9*, 2103930.
[12] A. Hu, W. Chen, X. Du, Y. Hu, T. Lei, H. Wang, L. Xue, Y. Li, H. Sun, Y. Yan, J. Long, C. Shu, J. Zhu, B. Li, X. Wang, J. Xiong, *Energy Environ. Sci.* **2021**, *14*, 4115.
[13] G. Yu, Y. Cui, S. Lin, R. Liu, S. Liu, Y. Zhu, D. Wu, *Adv. Funct. Mater.* **2024**, *34*, 2314935.
[14] S. Yao, Y. Yang, Z. Liang, J. Chen, J. Ding, F. Li, J. Liu, L. Xi, M. Zhu, J. Liu, *Adv. Funct. Mater.* **2023**, *33*, 2212466.
[15] R. Zhu, C. Zhu, N. Sheng, Z. Rao, Y. Aoki, H. Habazaki, *Chem. Eng. J.* **2020**, *388*, 124256.
[16] J. Cai, L. Wang, Q. Huang, W. Yu, C. Xie, Z. Zheng, *Adv. Energy Mater.* **2024**, *14*, 2303088.
[17] H. Kwon, J.-H. Lee, Y. Roh, J. Baek, D. J. Shin, J. K. Yoon, H. J. Ha, J. Y. Kim, H.-T. Kim, *Nat. Commun.* **2021**, *12*, 5537.
[18] J. Wang, M. Wang, F. Chen, Y. Li, L. Zhang, Y. Zhao, C. Chen, *Energy Storage Mater.* **2021**, *34*, 22.
[19] Y. Wang, J. Tan, Z. Li, L. Ma, Z. Liu, M. Ye, J. Shen, *Energy Storage Mater.* **2022**, *53*, 156.
[20] K. Yan, Z. Lu, H.-W. Lee, F. Xiong, P.-C. Hsu, Y. Li, J. Zhao, S. Chu, Y. Cui, *Nat. Energy* **2016**, *1*, 16010.
[21] W.-B. Jung, O. B. Chae, M. Kim, Y. Kim, Y. J. Hong, J. Y. Kim, S. Choi, D. Y. Kim, S. Moon, J. Suk, Y. Kang, M. Wu, H.-T. Jung, *ACS Appl. Mater. Interfaces* **2021**, *13*, 60978.
[22] C.-P. Yang, Y.-X. Yin, S.-F. Zhang, N.-W. Li, Y.-G. Guo, *Nat. Commun.* **2015**, *6*, 8058.
[23] F. Luo, D. Xu, Y. Liao, M. Chen, S. Li, D. Wang, Z. Zheng, *J. Energy Chem.* **2023**, *77*, 11.
[24] B. Wang, Y. Ren, Y. Zhu, S. Chen, S. Chang, X. Zhou, P. Wang, H. Sun, X. Meng, S. Tang, *Adv. Sci.* **2023**, *10*, 2300860.

[25] K. Tang, H. Gao, J. Xiao, M. Long, J. Chen, H. Liu, G. Wang, *Chem. Eng. J.* **2022**, *436*, 134698.
[26] C. Guo, Y. Guo, R. Tao, X. Liao, K. Du, H. Zou, W. Zhang, J. Liang, D. Wang, X.-G. Sun, S.-Y. Lu, *Nano Energy* **2022**, *93*, 106831.
[27] Y. Fan, J. Liao, D. Luo, Y. Huang, F. Sun, J. Nan, *Chem. Eng. J.* **2022**, *453*, 139903.
[28] Y. Liu, X. Qin, S. Zhang, L. Zhang, F. Kang, G. Chen, X. Duan, B. Li, *J. Mater. Chem. A* **2019**, *7*, 13225.
[29] L. Zhang, X. Qin, S. Zhao, A. Wang, J. Luo, Z. L. Wang, F. Kang, Z. Lin, B. Li, *Adv. Mater.* **2020**, *32*, 1908445.
[30] S. J. An, J. Li, C. Daniel, D. Mohanty, S. Nagpure, D. L. Wood III, *Carbon* **2026**, *105*, 52.
[31] H. Wu, H. Jia, C. Wang, J.-G. Zhang, W. Xu, *Adv. Energy Mater.* **2021**, *11*, 2003092.
[32] Z. Yu, P. E. Rudnicki, Z. Zhang, Z. Huang, H. Celik, S. T. Oyakhire, Y. Chen, X. Kong, S. C. Kim, X. Xiao, H. Wang, Y. Zheng, G. A. Kamat, M. S. Kim, S. F. Bent, J. Qin, Y. Cui, Z. Bao, *Nat. Energy* **2022**, *7*, 94.
[33] P. A. G. O'Hare, G. K. Johnson, *J. Chem. Thermodyn.* **1975**, *7*, 13.
[34] W. Li, M. Li, S. Wang, P.-H. Chien, J. Luo, J. Fu, X. Lin, G. King, R. Feng, J. Wang, J. Zhou, R. Li, J. Liu, Y. Mo, T.-K. Sham, X. Sun, *Nat. Nanotechnol.* **2025**, *20*, 265.
[35] S. Ni, M. Zhang, C. Li, R. Gao, J. Sheng, X. Wu, G. Zhou, *Adv. Mater.* **2023**, *35*, 2209028.
[36] X. Li, Y. Su, Y. Qin, F. Huang, S. Mei, Y. He, C. Peng, L. Ding, Y. Zhang, Y. Peng, Z. Deng, *Adv. Mater.* **2023**, *35*, 2303489.
[37] X. Fu, M. J. Hurlock, C. Ding, X. Li, Q. Zhang, W.-H. Zhong, *Small* **2022**, *18*, 2106225.
[38] J. Ding, T. Du, E. H. Thomsen, D. Andresen, M. R. Fischer, A. K. Møller, A. R. Petersen, A. K. Pedersen, L. R. Jensen, S. Wang, M. M. Smedskjaer, *Adv. Sci.* **2024**, *11*, 2306698.
[39] Z. Chang, H. Yang, A. Pan, P. He, H. Zhou, *Nat. Commun.* **2022**, *13*, 6788.
[40] L.-Y. Yang, J. H. Cao, W. H. Liang, Y.-K. Wang, D.-Y. Wu, *ACS Appl. Mater. Interfaces* **2022**, *14*, 13722.
[41] W.-L. Wu, Y.-T. Xu, X. Ke, Y.-M. Chen, Y.-F. Cheng, G.-D. Lin, M.-P. Fan, L.-Y. Liu, Z.-C. Shi, *Energy Storage Mater.* **2021**, *37*, 387.
[42] Y.-G. Lee, S. Fujiki, C. Jung, N. Suzuki, N. Yashiro, R. Omoda, D.-S. Ko, T. Shiratsuchi, T. Sugimoto, S. Ryu, J. H. Ku, T. Watanabe, Y. Park, Y. Aihara, D. Im, I. T. Han, *Nat. Energy* **2020**, *5*, 299.
[43] H. J. Choi, D. W. Kang, J.-W. Park, J.-H. Park, Y.-J. Lee, Y.-C. Ha, S.-M. Lee, S. Y. Yoon, B. G. Kim, *Adv. Sci.* **2022**, *9*, 2103826.
[44] B. Cui, J. Xu, *J. Mater. Chem. A* **2025**, *13*, 8223.
[45] Y. Fan, R. Li, R. Yi, L. Zheng, J. Wang, R. Huang, Z. Gong, Z. Li, J. Qi, X. Fan, Y. Shen, L. Chen, *Cell Rep. Phys. Sci.* **2023**, *4*, 101324.
[46] S. Yang, M. Hu, X. Liang, Z. Xie, Z. Wang, K. Zhou, *J. Colloid Interface Sci.* **2024**, *646*, 886.
[47] J. Ding, T. Du, L. R. Jensen, S. S. Sørensen, D. Wang, S. Wang, L. Zhang, Y. Yue, M. M. Smedskjaer, *Adv. Mater.* **2024**, *36*, 2400652.
[48] T. Wakiya, Y. Kamakura, H. Shibahara, K. Ogasawara, A. Saeki, R. Nishikubo, A. Inokuchi, H. Yoshikawa, D. Tanaka, *Angew. Chem., Int. Ed.* **2021**, *60*, 23217.
[49] J. Yao, L. Liang, H. Chen, R. Tang, *Polyhedron* **2024**, *257*, 117015.
[50] C. Ma, Q. Qiao, K. Yue, J. Yue, X. Cai, J. Zheng, L. Kang, Y. Wang, J. Nai, J. Luo, H. Yuan, S. Zou, X. Tao, Y. Liu, *Adv. Funct. Mater.* **2024**, *34*, 2406479.
[51] Q. Zhang, L. Xu, X. Yue, J. Liu, X. Wang, X. He, Z. Shi, S. Niu, W. Gao, C. Cheng, Z. Liang, *Adv. Energy Mater.* **2023**, *13*, 2302620.
[52] J. Zhong, Z. Wang, X. Yi, X. Li, H. Guo, W. Peng, J. Wang, G. Yan, *Small* **2024**, *20*, 2308678.
[53] P.-C. Li, Z.-Q. Zhang, Z.-W. Zhao, J.-Q. Li, Z.-X. Xu, H. Zhang, G. Li, *Adv. Mater.* **2024**, *36*, 2406359.
[54] S. Zhao, Y. Li, H. Yin, Z. Liu, E. Luan, F. Zhao, Z. Tang, S. Liu, *Sci. Adv.* **2015**, *1*, 1500372.